



Basic Neuroscience

Automated quantification of neuronal networks and single-cell calcium dynamics using calcium imaging

Tapan P. Patel^a, Karen Man^a, Bonnie L. Firestein^b, David F. Meaney^{a,c,*}^a Department of Bioengineering, University of Pennsylvania, United States^b Department of Cell Biology and Neuroscience, Rutgers University, United States^c Department of Neurosurgery, University of Pennsylvania, United States

HIGHLIGHTS

- We present an open-source software for semi-automated analysis of fluorescent calcium imaging.
- FluoroSNNAP, Fluorescence Single Neuron and Network Analysis Package, enables automated segmentation and calcium transient event detections.
- Calcium dynamics of single-cells can be used to phenotype neurons.
- FluoroSNNAP enables global and local synchronization cluster analysis.
- FluoroSNNAP determines functional connectivity and allows graphical visualization.

ARTICLE INFO

Article history:

Received 15 July 2014

Received in revised form

30 November 2014

Accepted 18 January 2015

Available online 25 January 2015

Keywords:

Calcium imaging

Event detection

Functional connectivity

Synchrony

Neuronal phenotype

FluoroSNNAP

ABSTRACT

Background: Recent advances in genetically engineered calcium and membrane potential indicators provide the potential to estimate the activation dynamics of individual neurons within larger, mesoscale networks (100s–1000+ neurons). However, a fully integrated automated workflow for the analysis and visualization of neural microcircuits from high speed fluorescence imaging data is lacking.

New method: Here we introduce FluoroSNNAP, Fluorescence Single Neuron and Network Analysis Package. FluoroSNNAP is an open-source, interactive software developed in MATLAB for automated quantification of numerous biologically relevant features of both the calcium dynamics of single-cells and network activity patterns. FluoroSNNAP integrates and improves upon existing tools for spike detection, synchronization analysis, and inference of functional connectivity, making it most useful to experimentalists with little or no programming knowledge.

Results: We apply FluoroSNNAP to characterize the activity patterns of neuronal microcircuits undergoing developmental maturation *in vitro*. Separately, we highlight the utility of single-cell analysis for phenotyping a mixed population of neurons expressing a human mutant variant of the microtubule associated protein tau and wild-type tau.

Comparison with existing method(s): We show the performance of semi-automated cell segmentation using spatiotemporal independent component analysis and significant improvement in detecting calcium transients using a template-based algorithm in comparison to peak-based or wavelet-based detection methods. Our software further enables automated analysis of microcircuits, which is an improvement over existing methods.

Conclusions: We expect the dissemination of this software will facilitate a comprehensive analysis of neuronal networks, promoting the rapid interrogation of circuits in health and disease.

© 2015 Published by Elsevier B.V.

1. Introduction

Recent advances in medical imaging allow researchers to study the macroscopic structural and functional organization of the brain with remarkable detail, characterizing broad changes in brain connectivity that occur over several seconds as individuals perform a cognitive task (Matthews et al., 2006; Sorbara et al., 2012; Toga

* Corresponding author at: Department of Bioengineering, 240 Skirkanich Hall, 210 S, 33rd Street, Philadelphia, PA 19104-6321, United States.

Tel.: +1 215 573 2726; fax: +1 215 573 2071.

E-mail address: dmeaney@seas.upenn.edu (D.F. Meaney).

et al., 2006). In addition, local field potentials recorded with multi-electrode arrays provide much more precise temporal resolution to estimate local activation dynamics in a specific brain region during task performance. Advances in network theory are now showing that features of the neural circuitry between these two length scales – i.e., the distribution of neuronal connections in a network, and the clustering of these connections to form functional modules or microcircuits – are key variables that affect information flow through the network, the synchronization of activity across neuronal clusters, and the network activity patterns that can emerge from the network (Kohar et al., 2014; Liu et al., 2011; Pandit and Amritkar, 1999; Watts and Strogatz, 1998). However, developing more precise, circuit-based understanding of task performance at this intermediate scale remains elusive, partly because we have limited ability to characterize the functional connections of neurons within a microcircuit and how these connections are modified during cognition.

Technological advances in optical probes provide an opportunity to probe brain function and map brain networks with single neuron resolution, developing connection maps that can contain more than ~1000 neurons. Both calcium- and voltage-sensitive fluorescence indicators (Akerboom et al., 2012; Gong et al., 2014; Jin et al., 2012; Tian et al., 2009; Zariwala et al., 2012) allow simultaneous recording of large populations of neurons to estimate neural activity patterns with near single cell resolution rather than relying on field potentials measured with microelectrode arrays to infer activity of small populations of neurons (Akerboom et al., 2012; Cossart et al., 2005). Neuroscientists can use these new optical reagents to record the spontaneously generated or stimulus-evoked activity of a microcircuit both *in vitro* and *in vivo*, providing broad applicability in neuroscience (Adams et al., 2011; Bathellier et al., 2012; Takahashi et al., 2010). Moreover, a new generation of genetically encoded calcium and membrane potential indicators provides long term estimates of the neural activity patterns within the same neuronal ensemble over weeks to months (Ghosh et al., 2011; Ziv et al., 2013). In parallel with these advances in imaging probes, new techniques rooted in both graph theory and signal processing are now available to the neuroscience community for analyzing the large amounts of data generated by these indicators in microcircuits (Rubinov and Sporns, 2010; Sporns, 2013). However, these tools are often developed for a specific application within a laboratory and frequently lack a user-friendly interface for broader dissemination among laboratories. As a result, the barrier for experimentalists to use many of these newly developed technologies remains high.

To significantly reduce the technological barrier and make this microcircuit imaging more available to the neuroscience community, we introduce FluoroSNNAP, Fluorescence Single Neuron and Network Analysis Package, to aid in the analysis of high speed calcium imaging data acquired from intact microcircuits *in vitro*. We adapted and improved on existing tools for automatically computing numerous biologically relevant features of neuronal network activity. In addition, we created a graphical user interface (GUI) to streamline the processing and visualization of both single cell and network parameters. The software is implemented in MATLAB (MathWorks, Inc.) and does not use proprietary libraries, APIs or specialized toolboxes. It can be downloaded from www.seas.upenn.edu/molneuro/fluorosnnap.html. Since FluoroSNNAP does not require any programming knowledge, it will be especially useful to neuroscientists who want to use calcium or voltage imaging as a functional tool to estimate microcircuit properties following an experimental manipulation. The software can be used for the simple visualization of an individual neuronal response over time and comparing fluorescence dynamics among neurons within a specific circuit. Alternatively, this software toolkit can be used to complete a more complex synchronization

analysis to identify different patterns of network activity and inter-actively explore the functional connectivity of a microcircuit. We used FluoroSNNAP in two separate applications that required the examination of both the network structure and the single cell calcium dynamics (SCCD) phenotypes. First, we used a network-level analysis to study how developmental maturation of neurons grown in culture influence patterns of spontaneous activity. Second, we used automatically derived measures of single-cell calcium dynamics to phenotype a mixed population of neurons expressing either wildtype or mutant variant of the human microtubule-associated protein tau. Together, these applications demonstrate the utility of the developed software to analyze neural circuits with more ease than previously possible.

2. Methods

2.1. Cell culture

All animal procedures were approved by the University of Pennsylvania Institutional Animal Care and User Committee. Embryos at day E18 were surgically removed from a timed pregnant Sprague-Dawley rat anesthetized with 5% CO₂ and sacrificed *via* cervical dislocation. Neocortical tissue was dissected from the embryos and dissociated for 15 min at 37 °C in trypsin (1.4 mg/mL) and DNase (0.6 mg/mL, Roche Applied Science, Indianapolis, IN). After trituration and filtration through Nitex mesh (Crosswire Cloth, Bellmawr, NJ), cells were resuspended in MEM with Earl's salts and GlutaMAX supplemented with 0.6% D-glucose (Sigma–Aldrich, St. Louis, MO), 1% Pen-Strep, and 10% Horse Serum and plated on poly-D-lysine- (0.08 mg/mL, Sigma–Aldrich) and laminin- (0.001 mg/mL BD Biosciences, San Jose, CA) coated glass bottom dishes (MatTek, Ashland, MA). Cells were plated at a density of 200,000 cells/mL, roughly 10,000 cells/mm². After overnight adhesion, medium was replaced with Neurobasal medium supplemented with B-27 and 0.4 mM GlutaMAX and grown in a humidified 37 °C 5% CO₂ incubator.

For experiments involving mixed neuronal populations containing the expression of mutant variant of the human microtubule-associated protein tau (P301S) and wildtype tau, we crossed a PS19 monogenic female mouse expressing P301S mutant tau (Yoshiyama et al., 2007) to a wildtype male and isolated hippocampal neurons from the embryonic litter. Hippocampi of 7–10 embryos from the same litter were dissociated together and plated onto MatTek dishes as described above, which yielded a mixed population of neurons that contained either monogenic P301S tau or only wildtype tau.

2.2. Calcium imaging and data acquisition

For calcium imaging using the synthetic calcium indicator Fluo-4, a vial of 50 µg Fluo4-AM (Invitrogen F-14201) was solubilized with the non-ionic surfactant Pluronic F-127 in 20% DMSO (Invitrogen, P-3000MP) to yield a 1 mM stock solution. The stock solution was further diluted in controlled saline solution (CSS) to 2 µM (CSS: in mM, 126 NaCl, 5.4 KCl, 1 MgCl₂*6H₂O, 1.8 CaCl₂*2H₂O, 10 HEPES, 25 glucose). Osmolarity of CSS was adjusted to 290 mOsm and pH to 7.4. The culture medium was exchanged with 2 mL CSS, and the cultures were loaded with Fluo-4AM for 30 min. The cultures were rinsed gently in CSS before imaging.

Intracellular [Ca²⁺] was determined from fluorescence intensity using the formula

$$[\text{Ca}^{2+}] = \frac{F - F_{\min}}{F_{\min} - F} * K_d \quad (1)$$

where F is the fluorescence intensity, F_{\min} was determined by imaging neurons in a calcium free saline solution and F_{\max} was

determined by imaging neurons in normal saline solution, containing 5 μ M ionomycin (Sigma–Aldrich). K_d for Fluo-4 was 345 nM.

For calcium imaging with a genetically engineered calcium indicator (GECI), neurons were transduced at least 7 days prior to planned imaging study with an adeno-associated virus expressing GCaMP6f under the control of the synapsin-1 promoter (Chen et al., 2013) (Penn Vector Core #AV-1-PV2822, GC 5.92*10⁹).

Images of spontaneous calcium activity were acquired with a Nikon Eclipse TE2000U microscope fitted with a spinning disk confocal (CSU-10b, Solamere Technologies), a CCD camera (Photometric Cool-Snap HQ2, BioVision, Exton PA), 488-nm excitation laser (Prairie SFC), and a Nikon 10X Plan Apo objective (N.A. = 0.4). Exposure time was set to 50 ms, and images were streamed at 20 Hz frame rate for at least 5 min. Each image frame was 520 \times 696 pixels, which corresponded to 0.3 mm² rectangular area.

2.3. Immunocytochemistry

Following calcium imaging experiments, neurons were fixed with 4% paraformaldehyde in phosphate-buffered saline and probed for the presence of human P301S tau using rabbit polyclonal 17025 antibody (generously provided by Dr. Virginia Lee) per standard protocol. Briefly, cells were permeabilized with 0.2% Triton X-100 for 10 min, blocked in 5% normal goat serum (NGS) for 30 min, incubated with 17025 primary antibody in NGS overnight, and immunostained with Alexa Fluor goat anti-rabbit 594 secondary. Images were acquired on an upright Leica SP5 confocal microscope with a 25 \times objective (N.A. 0.95) and rotated 90 $^\circ$ to match the coordinate system of calcium images. Markers placed on the bottom of the glass cover slip prior to calcium imaging helped navigate to the same field of view. We manually co-registered the immunofluorescence image of fixed neurons to a fluo-4 image of the same field of view to retrospectively identify neurons that expressed the transgene.

2.4. Data analysis

Analysis of calcium fluorescence images is achieved through an interactive Fluorescence Single Neuron and Network Analysis Package (FluoroSNNAP) designed in MATLAB (release 2014a, MathWorks, Inc., Natick, MA). The entire software package and sample experiments can be downloaded from www.seas.upenn.edu/molneuro/fluorosnnap.html.

The general workflow is outlined in Fig. 1 and detailed below. Briefly, the steps are as follows: (1) identify cell somata (neuron) in an image (segmentation), (2) compute a time-varying fluorescence trace for each neuron across the image stack, (3) detect the onset of calcium transients (event detection), (4) quantify the shape and characteristics of calcium events for each neuron (phenotype), and (5) compute the synchronization and functional connectivity of the network. We minimized user interaction by automating each step in the workflow but allowed user flexibility to interactively explore the raw and processed data and make manual corrections if needed.

Segmentation: A key first step in analysis is to identify cell bodies or regions of interest (ROIs) in an image frame. Often, it is difficult to manually draw ROIs around individual neurons because cell bodies *in vivo* are packed together, and the expression of genetically encoded calcium indicators is restricted to the cytoplasm, necessitating careful delineation of cell edges. Rather, we integrated an automated cell identification method based on spatiotemporal independent component analysis into our workflow (Mukamel et al., 2009). Briefly, the algorithm uses spatial similarity of the fluorescence of groups of pixels and their temporal co-variation to identify “independent” sources of calcium signals. However, it cannot detect cells that do not spike or differentiate

cells that fire synchronously. It also identifies neuronal projections that may not be of interest to the user for network-level analysis. ICA-based segmentation is often a good first start nonetheless and few manual corrections are required to generate a complete segmentation. We built a segmentation interface where the user can adjust parameters of the ICA-based segmentation algorithm to generate a preliminary labeled image. The Segmentation GUI interface allows users to interact with each automatically defined ROI. The user can then delete neurites by thresholding on a circularity factor (defined as $(4\pi \cdot \text{area})/\text{perimeter}^2$) or delete individual ROIs by freehand selection. In addition, the user can manually draw ROIs or use the active contour method to automatically delineate the boundary of an ROI using a user provided seed point (Chan and Vese, 2001; Caselles et al., 1997). This provides flexibility, greatly speeds up manual correction of an automatically generated segmentation and makes manual segmentation from scratch feasible by eliminating the need to carefully freehand cell contours. The performance of our semi-automated segmentation algorithm was compared to human operator driven manual segmentation based upon a bright-field microscope image and repeated playing of the time-series movie.

Detecting single neuron fluorescence events: Given a stack of .tiff images containing time-lapse images of calcium fluorescence and an accompanying segmentation file that delineates neurons (ROIs) from background, we first computed a fluorescence vs. time trace for each neuron. All pixels within each ROI were averaged to give a single time course, and $\Delta F/F$ was calculated by subtracting each value with the mean of the lower 50% of previous 10-s values and dividing it by the mean of the lower 50% of previous 10-s values. The user can adjust the time window in the software. This normalized fluorescence trace ($\Delta F/F_0$) trace was characterized by a baseline that was periodically interrupted by calcium transients of varying amplitude and duration. These transient events are indicative of one or more action potential (AP) events occurring within an individual neuron (Akerboom et al., 2009; Dombeck et al., 2007; Greenberg et al., 2008; Kerr et al., 2005). Although past work shows that the firing rate of neurons can be extracted by deconvolution of the calcium fluorescence waveform (Yaksi and Friedrich, 2006), this requires a specialized calibration process that is unique for each live cell microscopy setup. As such, we did not include additional analyses to estimate either firing rate or number of APs within individual neurons. Rather, we focused our work on reliably detecting calcium transient events within each neuron and used the temporal arrangement of these events across neurons to estimate functional connectivity across neuronal networks. We emphasize that the inferred functional connectivity is different from the underlying structural connectivity, which is directed and weighted. However, the undirected functional connectivity provides useful information regarding the temporal interactions of neural elements.

Automated event detection is generally a difficult problem, and especially more difficult for neuronal calcium fluorescence data, because a given neuron may contain variable number of events. Moreover, individual transients may have different amplitudes, different durations, occur at irregular intervals, and may be buried in significant noise. We explored three different methodologies for event detection, providing each of these to the user in the software package. Our first method used a percentile based threshold (e.g., mean + 2*standard deviation of fluorescence) to detect peak events, but we discovered this methodology was not robust enough to correctly identify both small and large amplitude transients (Fig. 2A and B). Our second option employed a more sophisticated method inspired by an automated spike detection of EEG dataset using the continuous wavelet transform (Nenadic and Burdick, 2005). Wavelet transform decomposes a time-varying signal into its frequency and time components. Since

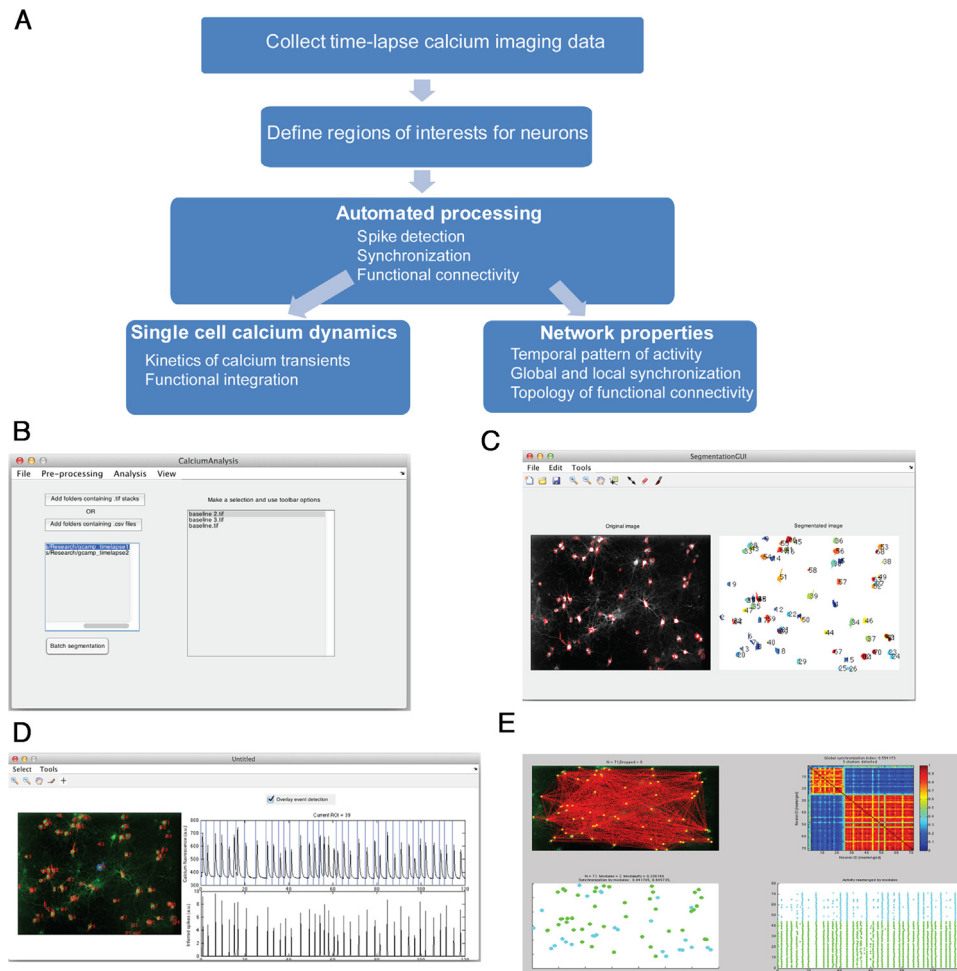


Fig. 1. Overview of image analysis. **A:** Workflow for the analysis of time-lapse calcium imaging. After acquiring images, pseudo-automated segmentation is performed to define regions of interest (ROIs), delineating neuronal somata from background. Fluorescence vs. time is computed for each ROI and the onsets of calcium transients are determined automatically. Single-cell features of calcium transients and network-level measures of synchrony and functional connectivity are computed. A graphical user interface was created to facilitate batch processing (**B**), segmentation (**C**), inspecting the fluorescence trace and spikes of individual neurons (**D**) and properties of the network (**E**).

spikes in EEG or calcium imaging transients in individual neurons are restricted to a certain range of frequencies, the wavelet transform can identify *when* these frequencies occur. Although this is conceptually simple, it required setting a number of empirical parameters to achieve good accuracy in practice. Often, it falsely identified events that were part of background noise and, more importantly, did not correctly identify the exact time of a transient (Fig. 2C and D). This time shift in event detection was a result of the limited temporal resolution of the wavelet transform, and was problematic because the precise timing of firing of neurons is an important parameter used to infer network connectivity.

To overcome these limitations, our third option for event detection used a previously described template-matching algorithm with a database of known transient waveforms (Schultz et al., 2009). The “peeling algorithm” described by Grewe et al. was not implemented as it requires knowledge of the calcium transient evoked by a single AP (which may not be generally available) and requires fine-tuning of multiple parameters for a Schmitt trigger and relies on simultaneous recordings of AP and calcium fluorescence (Grewe et al., 2010). Rather, we generalized the decisions that an observer made when identifying events in a time series. When manually identifying calcium events from imaging data, a user has some prior knowledge on the characteristics of calcium event, *i.e.*

its fast onset, exponential decay, short duration, and timing. Algorithmically, we constructed a database of transient waveforms by asking several observers to manually identify the onset and duration of calcium transients across multiple datasets. The criteria for calcium transient were abrupt rise in fluorescence followed by exponential decay and return to baseline fluctuation (Fig. 2E and F). To detect events in a time series, we computed the time-varying correlation coefficient between a ‘true’ calcium transient waveform – *i.e.* a waveform from the event database – and target fluorescence trace (Fig. 2G and H). We chose the correlation coefficient as our similarity metric because it is independent of amplitude, allowing us to identify a range of large and small transients (transients with amplitude $\Delta F/F_0 < 0.01$ were discarded as noise). Local maxima in the correlation-coefficient domain correspond to onset of calcium transients (Fig. 2I and J). A threshold correlation coefficient > 0.85 was used since it empirically optimized the tradeoff between maximizing the true positive rate and minimizing the false positive rate for our datasets and can be adjusted in the software.

Recognizing that the algorithm may sometimes falsely identify a transient or fail to detect a transient, we built an “Event Inspector” module where users can click on individual neurons in the field of view and inspect the raw fluorescence trace, overlaid with automatically identified events. The user can interactively delete falsely identified events or add events with simple mouse clicks.

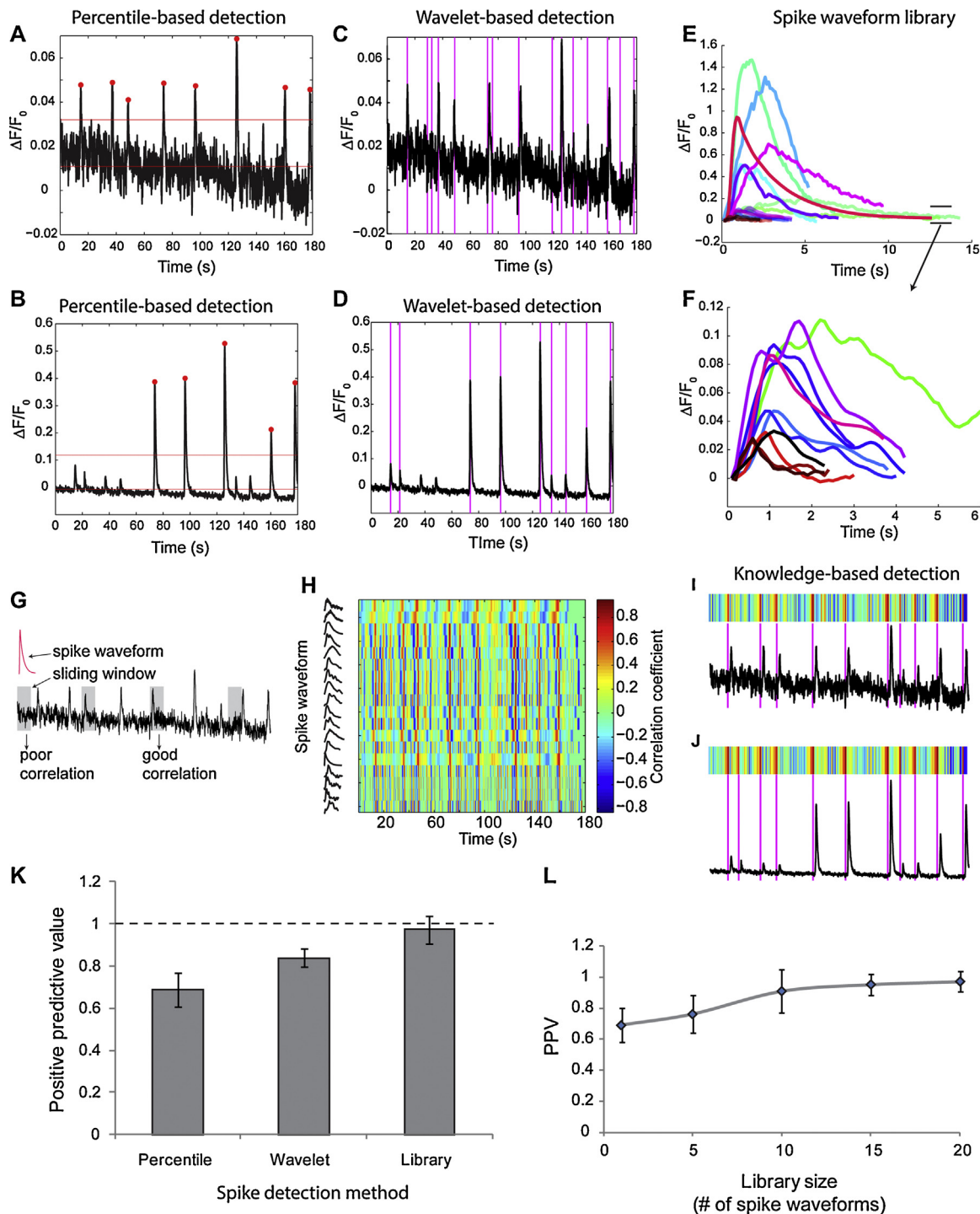


Fig. 2. Automated spike detection methodology. Percentile-based thresholding based on average fluorescence intensity for each region of interest (ROI) has positive predictive value of 86% for event detection if transient amplitude is nearly constant (A, example of an individual neuron's fluorescence trace) but fails to detect low amplitude calcium transients (PPV = 63%) when there are amplitude variations from spike-to-spike (B). Event detection using continuous-wavelet transform is an alternative, more sophisticated method. However, it suffers from high false positive rate when the signal to noise ratio is low (C, 34% false positives) and the wavelet transform can introduce small phase-shifts in the event times (D). A third method for event detection used a supervised algorithm by first building a database of unique calcium transient waveforms (E, F expanded view, note the different y-axes). Each waveform was used to generate a time-varying correlation trace that indicated the level of similarity between a true calcium transient and epochs of fluorescence trace (G; correlation value computed over 5 s windows, 100-ms displacement), generating a similarity matrix (H). Local maxima in the correlation matrix corresponded to the onset of calcium transients, providing a robust method for automated event detection for a noisy trace (I, heat map shows the maximum correlation coefficient across all spike waveforms) and a trace with varying amplitude (J). Across these three methodologies, the average fraction of true calcium transients that were correctly identified (PPV) was significantly higher for the supervised detection method when compared to either the percentile or wavelet transform based methods (K). The accuracy of supervised detection method was relatively insensitive to the number of true spike waveforms beyond $n = 10$ (L).

2.5. Single-cell calcium dynamics (SCCD) phenotyping module

We implemented several measurements to phenotype the temporal dynamics of calcium influx occurring within individual neurons. Overall, these measurements describe the spatiotemporal profile of calcium transients on a single neuron basis and can be a useful adjunct to changes in the network connectivity (Fig. 3). For each neuron identified with the segmentation tool, we provided measures of the following:

Baseline fluorescence: The baseline calcium fluorescence of a neuron is an indication of the intracellular free calcium concentration, $[Ca^{2+}]_i$, and is related to resting membrane potential, V_m . For example, removing tonic inhibitory drive with bicuculline raises V_m and increases $[Ca^{2+}]_i$ whereas a sodium channel blocker (TTX) slightly decreases V_m and $[Ca^{2+}]_i$. We computed the baseline fluorescence of each neuron by averaging parts of the fluorescence trace that are at least 2 s before and 10 s after the onset of a calcium transient.

Distribution of transients: The number of calcium events per neuron and the distribution of inter-event-interval (IEI) are important measures of the level of activity and rhythmicity. We report the mean and standard deviation of the IEI distribution for each neuron.

Kinetics of transients: The shape of a calcium transient is influenced by many factors, including the number and frequency of action potentials, the activation of synaptic sources of calcium entry, and the neuronal buffering capacity. We measured the amplitude, rise time, and fall time of each calcium event and their coefficient of variation (Fig. 3A). The amplitude was defined as the maximum change in fluorescence over baseline following the onset of a calcium transient. Rise time was defined as the time required to reach half maximal amplitude. Similarly, fall time was determined by fitting an exponentially decaying curve to the calcium transient. An $R^2 > 0.9$ indicated acceptable regression fit. When regression failed ($R^2 < 0.9$), we interpolated the time to reach half maximal amplitude during the decay part of the calcium transient. We also computed the coefficient of variation of the amplitudes of calcium transient as a measure of peak-to-peak variability, indicative of variable AP firing rates.

2.6. Network analysis module

Neural circuits display complex spontaneous and stimulus-evoked temporal activity patterns. As the calcium transients within individual neurons reflect one or more action potential events, the temporal matching of calcium transients among neurons provides an opportunity to characterize network structure. We used the temporal correspondence of events among neurons to infer ‘functional connectivity’ between neurons. We assembled these measures of functional connectivity across all neuron pairs in the network to establish an estimate of network structure. As many neurodegenerative and neuropsychiatric disorders are associated with changes in the pattern of resting state activity, we envisioned these methods for estimating functional network connectivity could provide new descriptors of the progressive changes that occur in these diseases.

Synchrony: A prominent feature of dynamic interconnected systems is their ability to synchronize (Acebrón et al., 2005). *In vivo*, synchronization serves a more general role by binding groups of distributed neuronal assemblies into functional units so that these assemblies can transfer information more easily (Melloni et al., 2007; Uhlhaas et al., 2008; Uhlhaas and Singer, 2006; Womelsdorf et al., 2007). To identify groups neurons with similar pattern of activity and to quantify their synchrony, we use an approach based on the instantaneous phase of the raw fluorescence time series. Separating a time-varying signal into its amplitude and phase components allow us to focus on the *timing* of events, regardless of its

amplitude. Phase synchronization has many features that make it attractive to the analysis of neuronal signals: (a) it can capture non-linear dependencies between two or more time series (overcoming limitations of cross-correlation), (b) it is time-resolved (overcoming limitations of coherence), (c) it does not rely on estimating probability distributions which is often a limiting step for synchronization methods based on mutual information or transfer entropy, and (d) the analysis can be restricted to specific frequency ranges, reflecting brain rhythms. Broadly, phase synchronization of signals across microcircuits could reveal important computational properties of brain regions during working tasks and cognition (Axmacher et al., 2006; Gregoriou et al., 2009; Tsubo et al., 2013). Therefore, a module for phase synchronization analysis offers an opportunity to determine if circuits show periods of enhanced synchronization, and if the addition of pharmacological agents, trophic factors, or circuit stimulation will affect the synchronization of these circuits.

To quantify the phase synchronization of two time series, $x(t)$ and $y(t)$, we first compute their instantaneous phase $\phi_x(t)$ and $\phi_y(t)$. The Hilbert transform or a Morlet wavelet transform have been used in the past for obtaining instantaneous phase; however, these techniques are sensitive to noise and require filtering the signal, which can potentially introduce unwanted phase shifts. Instead, we numerically compute instantaneous phase using calcium spike times where a neuron undergoes a full oscillatory cycle (phase angle = 0 to 2π) from one spike event to the next. Mathematically, the unwrapped instantaneous phase is given by:

$$\phi(t) = 2\pi * \frac{t - t^{(k)}}{t^{(k+1)} - t^{(k)}} + 2\pi k \quad (2)$$

where $t^{(k)}$ is the spike time of the k th spike.

If $x(t)$ and $y(t)$ are completely synchronized, their absolute phase difference $\psi_{x,y}(t) = \text{mod}(|\phi_x(t) - \phi_y(t)|, 2\pi)$ would be a constant. Alternatively, if $x(t)$ and $y(t)$ are completely independent, $\psi_{x,y}(t)$ will take on all values in the interval $[0, 2\pi]$. The distribution of $\psi_{x,y}(t)$ will be peaked at some phase-locked value in the former case and uniform in the latter case. The ‘‘peakiness’’ of a distribution can be quantified by its entropy and has been used as a measure of synchrony in some reports. However, this method requires normalizing and is sensitive to sample size and choice of bins across the phase range. Instead, we use a definition of pair-wise phase synchronization index, $\gamma_{x,y}$, based on circular variance of $\psi_{x,y}(t)$ given by

$$\gamma_{x,y} = \sqrt{(\langle \cos \psi_{x,y}(t) \rangle)^2 + (\langle \sin \psi_{x,y}(t) \rangle)^2} \quad (3)$$

where brackets denote average over time.

Geometrically, $\gamma_{x,y}$ measures the variability in the distribution of $\psi_{x,y}(t)$ when projected onto a unit circle. By definition, $\gamma_{x,y}$ takes on values in the interval $[0, 1]$; $\gamma_{x,y} = 1$ if $x(t)$ and $y(t)$ are perfectly synchronized and 0 if they are completely independent. $\gamma_{x,y}$ is also a proper distance metric, *i.e.* it is positive definite and satisfies the triangle inequality. This will be an important feature for cluster analysis described below.

To identify patterns of network activity, we computed pair-wise synchronization index of each neuron and populated a synchronization matrix \mathbf{S} of size $M \times M$, where M = number of neurons in the network. The synchronization matrix element ($\mathbf{S}(i,j)$) is the pair-wise synchronization index for the i th and j th neuron time series. Matrix formulation allowed us to use eigen decomposition to cluster groups of neurons that display similar activity patterns and to quantify the level of synchronization in each cluster. For complete mathematical details see (Allefeld et al., 2007; Bialonski and Lehnertz, 2006; Li et al., 2010). Briefly, the clustering algorithm relied on examining the distribution of the eigenvalues of the matrix \mathbf{S} . Given that \mathbf{S} is symmetric and positive-definite, we are guaranteed to have M real eigenvalues, $\lambda^{(M)}$. If all neurons were

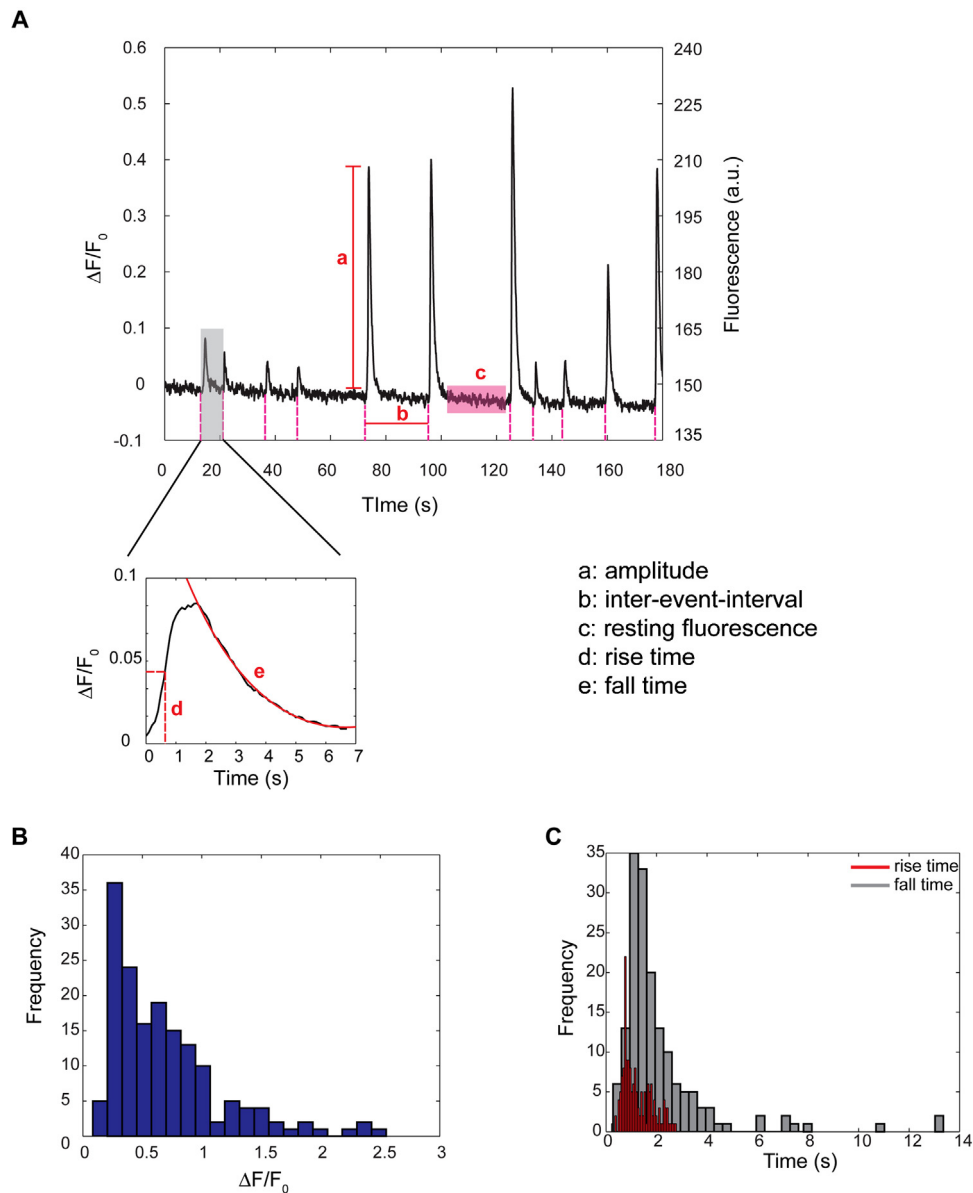


Fig. 3. Classifiers for single cell calcium dynamics of neurons in the network. **A:** Fluorescence vs. time trace depicts automated detection of calcium transients (pink dashed lines). For each transient, the peak amplitude (a), rise time (d) and fall time (e) are determined. The resting fluorescence of each cell (c) and mean inter-event-interval (b) are also automatically computed. The resulting normalized peak intensity for an individual neuron shows a distribution of values across a network (B), while the rise and fall times show a more uniform range of values (C, red bars – rise time; gray bars – fall time). (For interpretation of the references to color in figure legend, the reader is referred to the web version of the article.)

completely synchronized, there would be only 1 pattern of activity and all elements of the \mathbf{S} matrix would be identical ($=1$). In this case, there would only be one eigenvalue that is disproportionately larger than the rest, $\lambda_1 = \lambda_2 = \lambda_{M-1} = 0$, and $\lambda_M = M$. Alternatively, if all neurons fired independently and there was no organized pattern of activity, all elements of \mathbf{S} would be 0 and all eigenvalues would be identical, $\lambda_1 = \lambda_2 = \lambda_M = 0$. The number of disproportionately large eigenvalues corresponds to the number of unique activity patterns, and their corresponding eigenvectors contain information about which sets of neurons contribute to the creation of distinct patterns of activity. The largest eigenvalue is also proportional to the global synchronization index. We automatically computed pair-wise synchronization matrix and performed a synchronization cluster analysis as part of the workflow. The synchronization matrix and the raster plot of activity were rearranged based on their participation in a cluster and displayed for quick visual inspection of

unique patterns of activity. Note: synchronization analysis assumes that the state of neural systems does not change over the course of the imaging session.

Functional connectivity: A key utility of calcium imaging is the inference of functional connectivity, which we generally define as a strong temporal correspondence of events between two neurons. Fig. 4 highlights key steps in estimating functional connectivity of a population of neurons; the fluorescence trace of 4 neurons labeled in Fig. 4A are shown in Fig. 4B and these 4 traces are used to illustrate the algorithm for estimating functional connectivity. The simplest method to assess temporal relationships for calcium fluorescence time series of two neurons, $x(t)$ and $y(t)$, is through Pearson's correlation or cross-correlation (Fig. 4C). However, these operations are limited to linear interactions and require the use of an arbitrary threshold to determine functional connectivity. To avoid these shortcomings, we used surrogate data and statistical

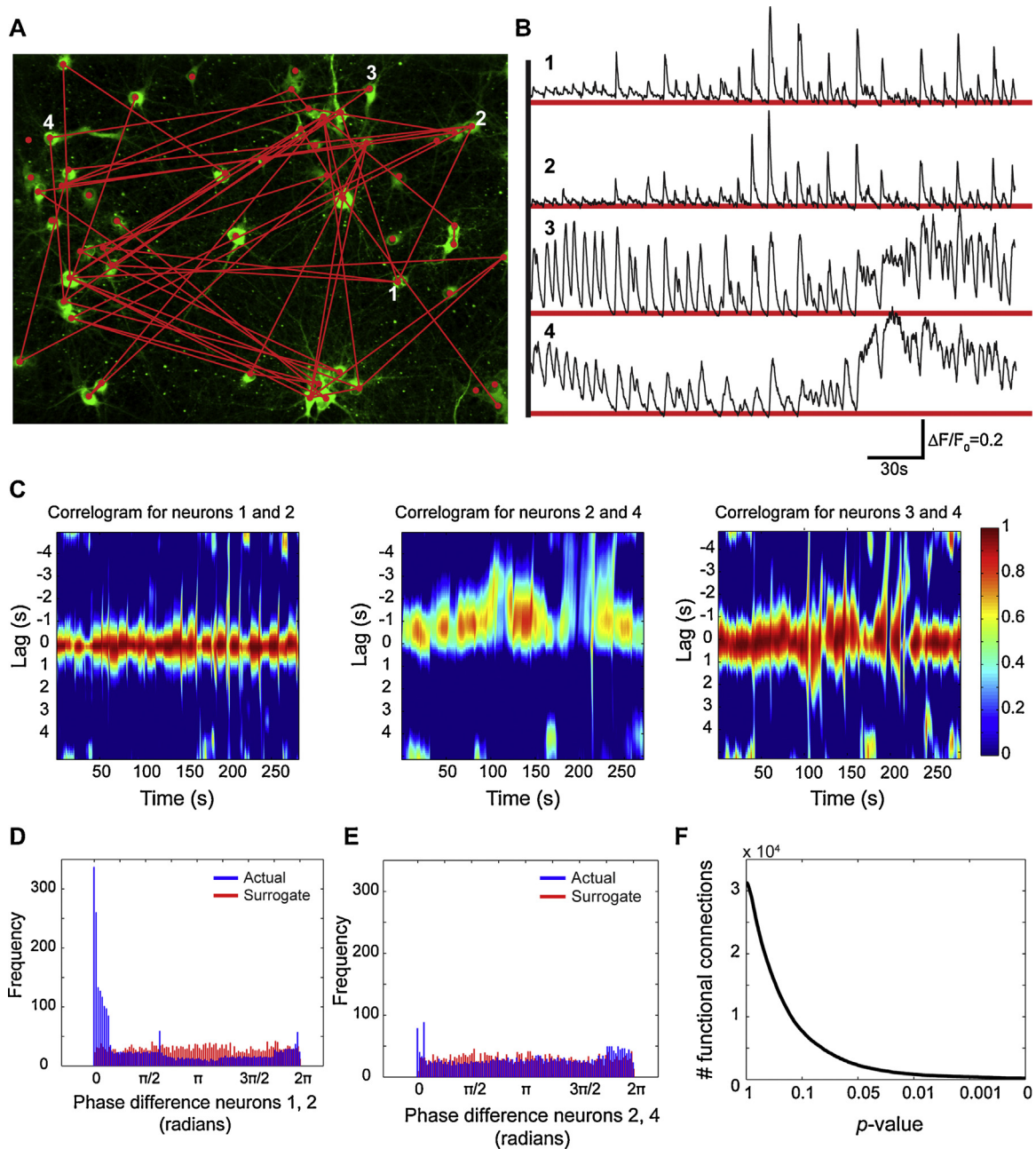


Fig. 4. Estimate of functional connectivity. The functional connectivity of pair-wise neurons (red lines, A) was determined by testing for statistical dependencies in their calcium activity. Visual inspection (B) and correlogram (C) of the fluorescence trace of 4 neurons indicated in A shows temporal similarity between neuronal pairs (1,2) and (3,4) but not between the pair (2,4). The distribution of instantaneous phase difference between pair-wise neurons was compared to the distribution generated by resampling the fluorescence trace of one of neuron pairs (D, E; blue bars – phase difference of actual; red bars – phase difference of surrogate). An overlap in the distributions of actual and surrogate samples is indicative of a lack of functional dependency. Kolmogorov–Smirnov test was used to test statistical similarity of the two distributions. A p -value < 0.01 was used as a threshold to infer functional connection; stricter statistical criteria did not change significantly the total number of functional connections beyond this point (F). (For interpretation of the references to color in figure legend, the reader is referred to the web version of the article.)

inference to determine functional connectivity. Given $x(t)$, $y(t)$, and their instantaneous phase $\phi_x(t)$, $\phi_y(t)$, our goal was to determine if the distribution of the instantaneous phase difference $\psi_{x,y}(t)$ was statistically significant. Since we did not know the null distribution H_0 a priori, we used amplitude adjusted Fourier transform (AAFT) of $y(t)$ to generate surrogate time series, $\hat{y}(t)$ and derived $\hat{\phi}_y$ and $\widehat{\psi}_{x,y}(t)$. The surrogate time series $\hat{y}(t)$ had the same linear correlation structure, power spectrum and the marginal distribution as $y(t)$ but was otherwise random. In contrast to random permutation, which destroys any possible correlations in the time series, AAFT is an autoregressive approach, and was used to test the null

hypothesis that the time series was generated by a Gaussian process undergoing a monotonic static transform, i.e. the changes in fluorescence of $y(t)$ are a result of spontaneous presynaptic release events and not influenced by the activity of $x(t)$. We used the Kolmogorov–Smirnov test to determine statistical departure of $\psi_{x,y}(t)$ from the surrogate time series $\widehat{\psi}_{x,y}(t)$ and chose $\alpha = 0.05$ and $p < 0.001$ to define a functional connection between neurons x and y (Fig. 4D–F).

We used routines from the Brain Connectivity Toolbox (Rubinov and Sporns, 2010) to describe the topology of the network using parameters that included modularity, clustering coefficient, and

path length. We also created an interactive interface to aid in data exploration and data mining. Selecting a neuron raises the focus of its functional targets, highlights their connections and provides detailed information about that neuron's single-cell and network properties, including the mean amplitude, inter-event-interval, rise and fall time, functional connectivity index, synchronization participation index, and nodal clustering coefficient.

3. Results

3.1. Interactive software for the automated phenotyping of neurons and quantification of neuronal network dynamics using calcium imaging

We developed a comprehensive and easy-to-use workflow for the analysis and interactive visualization of calcium activity of neuronal populations. Our software automatically extracts numerous biologically relevant and quantifiable features that described the activity and functional connectivity of a neuronal microcircuit. The overall workflow, depicted in Fig. 1, automated cell somata identification in an image (ROIs), calculated a time-varying fluorescence trace for each cell, detected the onset of calcium transients, and characterized single-cell and network-level features of calcium dynamics, synchronization, and functional integration.

3.2. Semi-automated segmentation of cell somata

We incorporated both human operator ROI selection and a modified spatio-temporal independent component analysis (stICA) (Mukamel et al., 2009) to delineate cell somata from background. Manual segmentation, although flexible and accurate, was time consuming compared to stICA. stICA based segmentation, on the other hand, often detected dendritic or axonal processes and over-segmented the image. In practice, we found that the best results could be achieved by using a semi-automated approach where stICA provided a guide for manual correction. Segmenting $\sim 500 \times 700 \mu\text{m}$ field of view with nearly 300 cells required on average less than 2 min of user interaction.

3.3. Template-matching automated detection of calcium transients

A crucial first step in the analysis of calcium fluorescence data is delineating calcium transients from noise-based fluctuations in fluorescence. Several methods exist for event detection. A simple approach selects a threshold value based on some predefined percentile (e.g., mean + 2*standard deviation) and identifies events that cross the threshold. This approach was not robust enough to detect both small and large amplitude transients (Fig. 2A and B), yielding an optimum positive predictive value (PPV, the fraction of automatically detected events that are true positives) of 0.688 ± 0.08 across 22 randomly selected calcium traces, which contained 158 manually verified true spikes (Fig. 2K). In comparison, the continuous wavelet transform to identify events either falsely detected events in noisy calcium fluorescence traces (average signal to noise ratio of <5) or introduced small phase shifts when calcium transients were too broad or too narrow (Fig. 2C and D). As a result, the average PPV for the wavelet transform method was 0.8395 ± 0.041 across the same imaging experiments analyzed with the threshold-based event detection algorithm. Finally, a customized database of expert labeled calcium transient waveforms provided the necessary input for template-based transient detection algorithm, (Fig. 2E and F). Given a fluorescence trace, $F_i(t)$, we compared the instantaneous similarity of $F_i(t)$ to known event waveforms (Fig. 2G), generating a time-varying similarity trace for each event waveform (Fig. 2H).

Local maxima in the similarity matrix correctly identified the onset of calcium transients (Fig. 2I and J), yielding a significantly better PPV 0.972 ± 0.065 compared to the other two methods (Fig. 2K). For these tests, we used a library of 20 template candidates that exhibited most clear calcium transient characteristics, defined as a positive first derivative followed by an exponential decay with a positive second derivative. We next tested the sensitivity of our algorithm to the choice of event waveforms in the library by using 1, 5, 10, 15 or all 20 spike waveforms, chosen at random. We found that a library of just 10 event waveforms achieved a PPV of 0.91 ± 0.14 and correctly detected $89\% \pm 5\%$ of the total 158 calcium transients (Fig. 2L). In our implementation, users can build their own personalized template libraries to identify calcium transients that best suit their dataset.

We implemented several quantitative descriptors of calcium dynamics of single-cells (Fig. 3A). Interestingly, we found large variability in the distribution of peak calcium fluorescence amplitudes, ranging from $\Delta F/F_0 = 0.1$ –2.5, in spontaneously active neurons (Fig. 3B). Despite this large range, the variance in rise time and fall time of individual calcium transients was smaller, with a median rise time of 0.67 ± 0.3 s and a median fall time 1.7 ± 0.6 s (Fig. 3C).

We applied the *network analysis module* of our software to better characterize the repertoire of spontaneously generated activity patterns at different stages during developmental maturation of embryonically derived cortical neurons in culture. Separately, we used the *single cell phenotyping module* to investigate whether overexpression of a mutant variant of the human microtubule-associated protein tau disrupted the calcium homeostasis of neurons expressing the transgene and whether these neurons could be distinguished from wild-type based solely on the dynamics of calcium activity.

3.4. Developmental changes in the frequency and coordination of neuronal network activity

Embryonic neurons in cultures form synaptic connections and undergo many similar developmental changes in receptor composition and phenotypic maturation that occur *in vivo* (Lesuisse and Martin, 2002). We imaged the spontaneous calcium activity of a population of neurons throughout this maturation process, beginning on day 8 *in vitro* (DIV 8) through day 21 (DIV 21). The activity of a microcircuit from each imaging session was time aligned using a network-wide burst event (defined as $>50\%$ co-active neurons). The full raster plot of activity from DIV 8–21 is shown in Fig. 5A where each dot, color-coded by culture age, represents the onset of a calcium transient from a given neuron label assigned arbitrarily. Activity of young neurons (DIV 8–11) was infrequent (at the single-cell level) and uncoordinated across neurons at the network-level. There were few rhythmic transitions between uncoordinated activity and network-wide burst event. The number of network-wide events varied over time *in vitro* (Fig. 5B). The frequency of spontaneous activity rapidly increased over DIV 12–14, reaching its peak at DIV 14 and subsequently reaching a plateau over DIV 18–21 (Fig. 5A and B). The pattern of coordinated activity followed a similar trend; the activity of young neurons was uncoordinated but became highly synchronized by DIV 14 and settled to a plateau by DIV 18 (Fig. 5C and D). This evolution of network activity is consistent with the (simplistic) model that neurons in culture undergo a period of rapid synaptic growth and strengthening, followed by synaptic pruning, reaching the completion of developmental synaptic modification at ~ 18 DIV (Nakanishi and Kukita, 1998; Nakayama et al., 2005; Passafaro et al., 2003; Tetzlaff et al., 2010; Voigt et al., 2005). Emergence of synchrony and spontaneous activity is a complicated phenomenon that also depends on maturation of cell surface receptors, changes in ionic currents, and the relative balance between excitation and inhibition, to name a few (Klueva

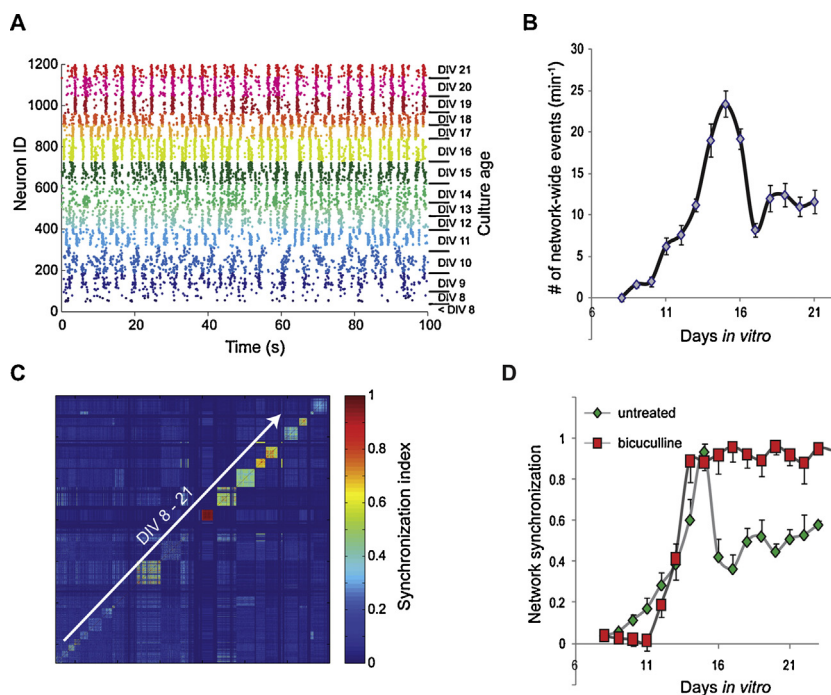


Fig. 5. Developmental changes in network activity patterns. **A:** Spontaneous activity patterns of neurons at different stages in development, colored-coded by age (days *in vitro*, DIV) and time-aligned for visual comparison, shows increasing frequency and greater complexity of activity as neurons mature. **B:** Network-bursts, recorded as simultaneous calcium transients in >90% of neurons in the imaging field of view, represent the transitions between synchronized and much less synchronized states of the network. The number of synchronized states per minutes gradually increased over development and reached its peak at DIV 14, consistent with increased synaptic growth and strength. This was followed by a significant decrease in the frequency of network bursts over DIV 15–16, and a plateau DIV 18+. **C:** The pattern of activity became increasingly synchronized as neurons matured in culture and reached its peak at DIV 14 as revealed by increasing “red” in the synchronization matrix. **D:** Beyond DIV 14, spontaneous activity was moderately synchronized, characterized by a mix of synchronized network-wide bursts and intermittent flickering events. Antagonizing the GABA_A receptor with bicuculline forced synchronized calcium oscillations in mature (DIV 14+) cultures because of recurrent excitation and network disinhibition. In comparison, bicuculline greatly reduced the frequency and coordination of activity in immature cultures (DIV 8–12). (For interpretation of the references to color in figure legend, the reader is referred to the web version of the article.)

et al., 2008; McCabe et al., 2006; Misonou et al., 2004; Opitz et al., 2002; Turrigiano et al., 1994).

In addition to the structural remodeling associated with developmental maturation, networks undergo a change in the balance of inhibition and excitation. In contrast to the mature brain, in which GABA is the major inhibitory neurotransmitter, in the developing brain GABA can be excitatory (Ben-Ari, 2002). We applied bicuculline, a GABA_A antagonist to neuronal cultures at different points in their development and measured the change in the frequency of calcium events and the synchronization of the network. In young cultures (DIV 8–11), bicuculline treatment significantly reduced excitatory activity and abolished synchrony. In contrast, exposure to bicuculline in older cultures (DIV 14+) significantly enhanced synchronized activity (Fig. 5D), consistent with previous reports indicating that GABA_A receptor activation is a major route of excitation in young neurons, primarily from the altered expression of chloride transporters KCC2 and NKCC1 (Fukuda et al., 1998; Ganguly et al., 2001; Rivera et al., 1999; Yamada et al., 2004).

3.5. Expression of mutant variant of human tau is associated with altered calcium homeostasis

As a separate application of our software, we investigated if the shape of calcium transients of individual cells can be used to develop functional neuron subgroups, or phenotypes, that can exist in a heterogeneous neuronal ensemble. We cultured mouse embryonic hippocampal neurons that contained a mixture of neurons containing either mutant human tau variant (P301S) or wildtype tau protein, derived from cross of PS19 transgenic mouse line with wildtype mouse. We imaged the spontaneous calcium activity of this microcircuit using the fluorescent calcium indicator, fluo-4

(Fig. 6A). The cultures were fixed and probed for P301S tau using 12025 antibody to identify neurons within the same microcircuit that expressed the transgene (Fig. 6B).

We extracted 4 relevant shape features from spontaneously generated calcium transients for a given neuron, which included fluorescence at the onset of a transient, F_0 , the peak amplitude of the transient, $\Delta F/F_0$, rise time, t_{rise} , and fall time, t_{fall} . Each calcium transient arose from a neuron expressing either transgenic or wt tau protein (Fig. 6C, representative trace from a single wt neuron and a PS19 expressing neuron is shown). We projected the dataset into a lower dimensional space spanned by the first 2 principal components that were derived from a linear combination of the 4 shape-based features (84% explained variability). Each dot in Fig. 6D is the projection of quantifiable features of a single calcium transient. We found that two clusters readily emerged in the principal component space. Given that a principal component analysis identifies the combination of the original variables that has the largest possible variation, the emergence of clusters or groups is highly suggestive of the presence of discriminating characteristics between calcium transients of P301S and wildtype neurons. PCA based clustering had 95% sensitivity and 89% sensitivity in discriminating wildtype from PS19 neurons. We found that the resting free intracellular calcium, $[Ca^{2+}]_i$, and peak calcium amplitude of P301S tau expressing neurons undergoing spontaneous activity were significantly larger compared to neurons expressing wildtype tau (P301S tau $\Delta F/F_0$: 0.059 ± 0.004 vs. wildtype 0.043 ± 0.002 , $p < 0.001$, $n = 54$; P301S tau $[Ca^{2+}]_i$: $128 \text{ nM} \pm 2.1 \text{ nM}$ vs. wildtype $95 \text{ nM} \pm 2.8$, $p < 0.001$). Although spontaneously generated calcium transients of transgenic neurons reached a higher peak amplitude, these transients were significantly shorter-lived, resulting in equal calcium load (area under the

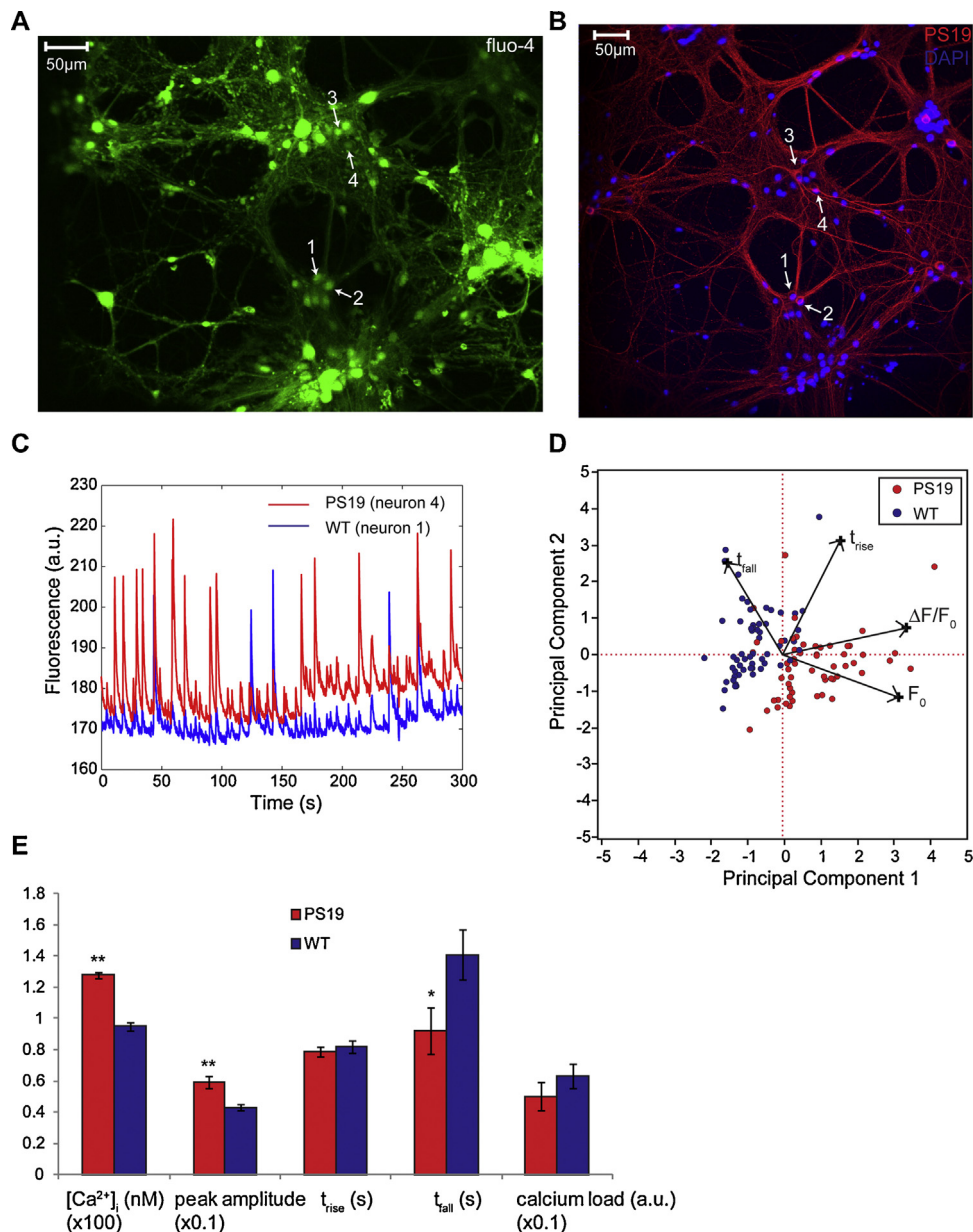


Fig. 6. Single-cell phenotypes revealed by calcium imaging. **A:** The spontaneous activity of mouse hippocampal neurons was recorded with the fluorescent calcium indicator, Fluo4-AM. Cultures were prepared with a mixture of neurons expressing either wildtype tau protein or a mutant version of human tau (P301S) **B:** Following calcium imaging, cells were fixed and probed for the expression of P301S tau protein with 12025 antibody (red – PS19, blue – DAPI). The same field of view used for calcium imaging was used during immunofluorescence microscopy to identify individual neurons that expressed the transgene (example of 4 co-registered neurons is indicated). **C:** Comparison of the average fluorescence trace of a representative neuron expressing the human mutant variant of tau (red) and wildtype neuron (blue) showed clear differences in the baseline fluorescence and amplitudes of calcium transients. **D:** Shape-based features of each calcium transient, including the fluorescence at the onset of a transient, peak amplitude, and characteristic rise and fall times, were computed and projected onto a 2-dimensional principal component space. Two clusters readily emerged in the principal component space, corresponding to neurons expressing mutant tau (red) or wild-type tau (blue). **E:** Resting $[Ca^{2+}]_i$ and peak amplitude were significantly larger in PS19 neurons and compared to wild-type. However, the duration of calcium transients was significantly shorter, resulting in similar calcium load between PS19 and WT neurons. PS19 $n=54$, WT, $n=53$. (** $p < 0.01$, * $p < 0.05$). (For interpretation of the references to color in figure legend, the reader is referred to the web version of the article.)

curve of calcium transients) for transgenic and wildtype neurons (P301S t_{fall} : 0.92 ± 0.15 s vs. wildtype: 1.41 ± 0.16 s, $p = 0.027$; P301S calcium load: 0.05 ± 0.009 vs. wildtype 0.063 ± 0.008 , $p > 0.05$). These alterations in the kinetics of calcium transients likely have an electrophysiological basis since expression of a different human mutant tau variant, P301L, has been shown to raise neuronal resting membrane potential, increase evoked action potential firing rate and decrease the duration of single action potentials (Rocher et al., 2010).

In addition to alterations in the kinetics of calcium transients, we used our software analysis module to identify if additional

features separated neurons expressing mutant protein from other neurons expressing wildtype protein. We found that the expression of P301S tau protein did not significantly change the pattern of network activity or the functional integration of these neurons in the network, likely because the fraction of neurons expressing the transgene was typically $< 10\%$ (data not shown).

Together, these data demonstrate the utility of our calcium imaging software in two broad applications – monitoring the temporal evolution of network activity and single-cell phenotyping using features extracted from the shape of spontaneously generated calcium transients.

4. Discussion

In this report, we present a comprehensive workflow for the automated analysis of single neuron and neuronal network properties using data acquired from *in vitro* or *in vivo* calcium imaging experiments. Functional multineuronal calcium imaging is becoming a more widely accessible and an important tool for measuring the effects of experimental manipulations on the activity of individual neurons and microcircuits. Many research groups use custom-coded algorithms for analyzing their data in different programming languages, and the output from one algorithm is not always easily integrated into analysis algorithms from other groups. These customized algorithms often create a technical barrier for many investigators to use these tools for interrogating microcircuit function. Our open-source software and the accompanying graphic user interface provide a single, comprehensive approach for the analysis of neuronal microcircuits.

We believe that this software significantly extends the repertoire of image-derived quantitative metrics of network function. To our knowledge, no commercial software exists for automated analysis of calcium imaging, and the only other publicly available software is limited to segmentation and measurement of fluorescence vs. time trace for each region of interest (Tomek et al., 2013). Several past reports use calcium imaging (and custom-coded analysis routines) to investigate the microarchitecture of local brain regions in anesthetized, awake, and task-engaged animals (Dombeck et al., 2007; Greenberg et al., 2008; Kerr et al., 2007, 2005; Petersen, 2007; Sato et al., 2007). Publicly available tools have already had a clear benefit in the analysis of fMRI, EEG, and electrophysiology data by offering research groups access to advanced routines and algorithms that go beyond the skills and expertise of an individual group (Cox, 1996; Cui et al., 2008; Delorme and Makeig, 2004; Duann et al., 2002; Meier et al., 2008; Quiroga et al., 2004; Spacek et al., 2008). The provided toolkit enables a more consolidated analysis of both the calcium transients and the corresponding estimates of circuit structure, extending the analysis to a wider community of investigators.

Some specific features of our toolkit were designed to improve upon existing methods. Unlike other reports that focus on detection of cell bodies in an image frame (segmentation) (Mukamel et al., 2009; Ozden et al., 2008; Tomek et al., 2013), our software automates the measurement of numerous biologically relevant features that relate to the function of both single neurons and networks. At the single neuron scale, we automatically detected the onset of $[Ca^{2+}]_i$ transients using a novel spike detection algorithm and measured the dynamics of each event, including peak amplitude, rise time, fall time, and resting fluorescence. With an improvement in detecting calcium transients among neurons, we incorporated a new algorithm for estimating circuit connectivity. In total, these improvements add to recent approaches for detecting the timing of calcium transients and the temporal correlation of events to estimate connections among neurons (Li et al., 2010; Lutcke et al., 2013; Mukamel et al., 2009; Orlandi et al., 2014; Stetter et al., 2012; Takahashi et al., 2010; Tibau et al., 2013). To increase usability, we also created several routines that allow interactive exploration of the dataset. Users can inspect the raw fluorescence trace of any arbitrary neuron in the field of view with a simple mouse click and examine the functional integration of the selected neuron to the rest of the network. Such level of exploration will be especially useful to investigate the role of particular neuronal subtypes or targeted gene manipulations on neuronal network function and dynamics of activity. We also created modules to remove falsely detected ROIs from the image series. Similarly, interactive adjustment of event detection threshold or modifications to the spike waveform library is possible, and both adjustments could improve

accuracy. However, we found that knowledge-based spike detection is accurate, even with a few spike waveforms.

The continual improvement in genetically engineered calcium indicators, coupled continual hardware improvements, will undoubtedly improve our ability to discern the functional connectivity with even more precision. Our methods developed will apply easily to these next generation indicators with little, if any, adjustment. Therefore, we expect the continued use of functional multineuronal calcium imaging, combined with our framework for analysis, will advance our understanding of how information flow within and across distributed brain networks drive behavior or contribute to disease manifestations.

Acknowledgements

Funding was provided by Department of Defense W911NF-10-1-0526, NIH PO1 NS 056202, NSF IOS-1353724, NJCBIR CBIR14IRG019, and NJCBIR multi-investigator grant CBIR12MIG011. We thank Jing Guo and Virginia M. Y. Lee (University of Pennsylvania) for providing PS19 ± neurons and 17025 antibody.

References

- Acebrón JA, Bonilla LL, Pérez Vicente CJ, Ritort F, Spigler R. The Kuramoto model: a simple paradigm for synchronization phenomena. *Rev Mod Phys* 2005;77:137.
- Adams BE, Kyi M, Reid CA, Myers DE, Xu S, Williams DA, et al. Seizure-like thalamocortical rhythms initiate in the deep layers of the cortex in a co-culture model. *Exp Neurol* 2011;227:203–9.
- Akerboom J, Chen TW, Wardill TJ, Tian L, Marvin JS, Mutlu S, et al. Optimization of a GCaMP calcium indicator for neural activity imaging. *J Neurosci* 2012;32:13819–40.
- Akerboom J, Rivera JD, Guilbe MM, Malave EC, Hernandez HH, Tian L, et al. Crystal structures of the GCaMP calcium sensor reveal the mechanism of fluorescence signal change and aid rational design. *J Biol Chem* 2009;284:6455–64.
- Allefeld C, Müller M, Kurths J. Eigenvalue decomposition as a generalized synchronization cluster analysis. *Int J Bifurc Chaos* 2007;17:3493–7.
- Axmacher N, Mormann F, Fernandez G, Elger CE, Fell J. Memory formation by neuronal synchronization. *Brain Res Rev* 2006;52:170–82.
- Bathellier B, Ushakova L, Rumpel S. Discrete neocortical dynamics predict behavioral categorization of sounds. *Neuron* 2012;76:435–49.
- Ben-Ari Y. Excitatory actions of gaba during development: the nature of the nurture. *Nat Rev Neurosci* 2002;3:728–39.
- Bialonski S, Lehnertz K. Identifying phase synchronization clusters in spatially extended dynamical systems. *Phys Rev E: Stat Nonlinear Soft Matter Phys* 2006;74:051909.
- Chan TF, Vese LA. Active contours without edges. *IEEE Trans Image Process: Publ IEEE Signal Process Soc* 2001;10:266–77.
- Chen TW, Wardill TJ, Sun Y, Pulver SR, Renninger SL, Baohan A, et al. Ultrasensitive fluorescent proteins for imaging neuronal activity. *Nature* 2013;499:295–300.
- Cossart R, Ikegaya Y, Yuste R. Calcium imaging of cortical networks dynamics. *Cell Calcium* 2005;37:451–7.
- Cox RW. AFNI: software for analysis and visualization of functional magnetic resonance neuroimages. *Comput Biomed Res* 1996;29:162–73.
- Cui J, Xu L, Bressler SL, Ding M, Liang H. BSMART: a Matlab/C toolbox for analysis of multichannel neural time series. *Neural Netw* 2008;21:1094–104.
- Delorme A, Makeig S. EEGLAB: an open source toolbox for analysis of single-trial EEG dynamics including independent component analysis. *J Neurosci Methods* 2004;134:9–21.
- Dombeck DA, Khabbaz AN, Collman F, Adelman TL, Tank DW. Imaging large-scale neural activity with cellular resolution in awake, mobile mice. *Neuron* 2007;56:43–57.
- Duann JR, Jung TP, Kuo WJ, Yeh TC, Makeig S, Hsieh JC, et al. Single-trial variability in event-related BOLD signals. *NeuroImage* 2002;15:823–35.
- Fukuda A, Muramatsu K, Okabe A, Shimano Y, Hida H, Fujimoto I, et al. Changes in intracellular Ca^{2+} induced by GABAA receptor activation and reduction in Cl⁻ gradient in neonatal rat neocortex. *J Neurophysiol* 1998;79:439–46.
- Ganguly K, Schinder AF, Wong ST, Poo M. GABA itself promotes the developmental switch of neuronal GABAergic responses from excitation to inhibition. *Cell* 2001;105:521–32.
- Ghosh KK, Burns LD, Cocker ED, Nimmerjahn A, Ziv Y, Gamal AE, et al. Miniaturized integration of a fluorescence microscope. *Nat Methods* 2011;8:871–8.
- Gong Y, Wagner MJ, Li JZ, Schnitzer MJ. Imaging neural spiking in brain tissue using FRET-opsin protein voltage sensors. *Nat Commun* 2014;5:3674.
- Greenberg DS, Houweling AR, Kerr JN. Population imaging of ongoing neuronal activity in the visual cortex of awake rats. *Nat Neurosci* 2008;11:749–51.
- Gregoriou GG, Gotts SJ, Zhou H, Desimone R. Long-range neural coupling through synchronization with attention. *Prog Brain Res* 2009;176:35–45.

- Grewe BF, Langer D, Kasper H, Kampa BM, Helmchen F. High-speed *in vivo* calcium imaging reveals neuronal network activity with near-millisecond precision. *Nat Methods* 2010;7:399–405.
- Jin L, Han Z, Platasa J, Wooltorton JR, Cohen LB, Pieribone VA. Single action potentials and subthreshold electrical events imaged in neurons with a fluorescent protein voltage probe. *Neuron* 2012;75:779–85.
- Kerr JN, de Kock CP, Greenberg DS, Bruno RM, Sakmann B, Helmchen F. Spatial organization of neuronal population responses in layer 2/3 of rat barrel cortex. *J Neurosci* 2007;27:13316–28.
- Kerr JN, Greenberg D, Helmchen F. Imaging input and output of neocortical networks *in vivo*. *Proc Natl Acad Sci U S A* 2005;102:14063–8.
- Klueve J, Meis S, de Lima AD, Voigt T, Munsch T. Developmental downregulation of GABAergic drive parallels formation of functional synapses in cultured mouse neocortical networks. *Dev Neurobiol* 2008;68:934–49.
- Kohar V, Ji P, Choudhary A, Sinha S, Kurths J. Synchronization in time-varying networks. *Phys Rev E: Stat Nonlinear Soft Matter Phys* 2014;90:022812.
- Lesuisse C, Martin LJ. Immature and mature cortical neurons engage different apoptotic mechanisms involving caspase-3 and the mitogen-activated protein kinase pathway. *J Cereb Blood Flow Metab: Off J Int Soc Cereb Blood Flow Metab* 2002;22:935–50.
- Li X, Ouyang G, Usami A, Ikegaya Y, Sik A. Scale-free topology of the CA3 hippocampal network: a novel method to analyze functional neuronal assemblies. *Biophys J* 2010;98:1733–41.
- Liu YY, Slotine JJ, Barabasi AL. Controllability of complex networks. *Nature* 2011;473:167–73.
- Lutcke H, Gerhard F, Zenke F, Gerstner W, Helmchen F. Inference of neuronal network spike dynamics and topology from calcium imaging data. *Front Neural Circuits* 2013;7:201.
- Matthews PM, Honey GD, Bullmore ET. Applications of fMRI in translational medicine and clinical practice. *Nat Rev Neurosci* 2006;7:732–44.
- McCabe AK, Chisholm SL, Picken-Bahrey HL, Moody WJ. The self-regulating nature of spontaneous synchronized activity in developing mouse cortical neurones. *J Physiol* 2006;577:155–67.
- Meier R, Egert U, Aertsen A, Nawrot MP. FIND – a unified framework for neural data analysis. *Neural Netw* 2008;21:1085–93.
- Melloni L, Molina C, Pena M, Torres D, Singer W, Rodriguez E. Synchronization of neural activity across cortical areas correlates with conscious perception. *J Neurosci* 2007;27:2858–65.
- Misonou H, Mohapatra DP, Park EW, Leung V, Zhen D, Misonou K, et al. Regulation of ion channel localization and phosphorylation by neuronal activity. *Nat Neurosci* 2004;7:711–8.
- Mukamel EA, Nimmerjahn A, Schnitzer MJ. Automated analysis of cellular signals from large-scale calcium imaging data. *Neuron* 2009;63:747–60.
- Nakanishi K, Kukita F. Functional synapses in synchronized bursting of neocortical neurons in culture. *Brain Res* 1998;795:137–46.
- Nakayama K, Kiyosue K, Taguchi T. Diminished neuronal activity increases neuron–neuron connectivity underlying silent synapse formation and the rapid conversion of silent to functional synapses. *J Neurosci* 2005;25:4040–51.
- Nenadic Z, Burdick JW. Spike detection using the continuous wavelet transform. *IEEE Trans Bio-Med Eng* 2005;52:74–87.
- Opitz T, De Lima AD, Voigt T. Spontaneous development of synchronous oscillatory activity during maturation of cortical networks *in vitro*. *J Neurophysiol* 2002;88:2196–206.
- Orlandi JG, Stetter O, Soriano J, Geisel T, Battaglia D. Transfer entropy reconstruction and labeling of neuronal connections from simulated calcium imaging. *PLOS ONE* 2014;9:e98842.
- Ozden I, Lee HM, Sullivan MR, Wang SS. Identification and clustering of event patterns from *in vivo* multiphoton optical recordings of neuronal ensembles. *J Neurophysiol* 2008;100:495–503.
- Pandit SA, Amritkar RE. Characterization and control of small-world networks. *Phys Rev E: Stat Phys Plasmas Fluids Relat Interdiscip Top* 1999;60:R1119–22.
- Passafaro M, Nakagawa T, Sala C, Sheng M. Induction of dendritic spines by an extracellular domain of AMPA receptor subunit GluR2. *Nature* 2003;424:677–81.
- Petersen CC. The functional organization of the barrel cortex. *Neuron* 2007;56:339–55.
- Quiroga RQ, Nadasdy Z, Ben-Shaul Y. Unsupervised spike detection and sorting with wavelets and superparamagnetic clustering. *Neural Comput* 2004;16:1661–87.
- Rivera C, Voipio J, Payne JA, Ruusuvuori E, Lahtinen H, Lamsa K, et al. The K⁺/Cl⁻ cotransporter KCC2 renders GABA hyperpolarizing during neuronal maturation. *Nature* 1999;397:251–5.
- Rocher AB, Crimins JL, Amatrudo JM, Kinson MS, Todd-Brown MA, Lewis J, et al. Structural and functional changes in tau mutant mice neurons are not linked to the presence of NFTs. *Exp Neurol* 2010;223:385–93.
- Rubinov M, Sporns O. Complex network measures of brain connectivity: uses and interpretations. *NeuroImage* 2010;52:1059–69.
- Sato TR, Gray NW, Mainen ZF, Svoboda K. The functional microarchitecture of the mouse barrel cortex. *PLoS Biol* 2007;5:e189.
- Schultz SR, Kitamura K, Post-Uiterweer A, Krupic J, Hausser M. Spatial pattern coding of sensory information by climbing fiber-evoked calcium signals in networks of neighboring cerebellar Purkinje cells. *J Neurosci: Off J Soc Neurosci* 2009;29:8005–15.
- Sorbara C, Misgeld T, Kerschensteiner M. *In vivo* imaging of the diseased nervous system: an update. *Curr Pharm Des* 2012;18:4465–70.
- Spacek M, Blanche T, Swindale N. Python for large-scale electrophysiology. *Front Neuroinform* 2008;2:9.
- Sporns O. Network attributes for segregation and integration in the human brain. *Curr Opin Neurobiol* 2013;23:162–71.
- Stetter O, Battaglia D, Soriano J, Geisel T. Model-free reconstruction of excitatory neuronal connectivity from calcium imaging signals. *PLoS Comput Biol* 2012;8:e1002653.
- Takahashi N, Sasaki T, Matsumoto W, Matsuki N, Ikegaya Y. Circuit topology for synchronizing neurons in spontaneously active networks. *Proc Natl Acad Sci U S A* 2010;107:10244–9.
- Tetzlaff C, Okujeni S, Egert U, Worgotter F, Butz M. Self-organized criticality in developing neuronal networks. *PLoS Comput Biol* 2010;6:e1001013.
- Tian L, Hires SA, Mao T, Huber D, Chiappe ME, Chalasani SH, et al. Imaging neural activity in worms, flies and mice with improved GCaMP calcium indicators. *Nat Methods* 2009;6:875–81.
- Tibau E, Valencia M, Soriano J. Identification of neuronal network properties from the spectral analysis of calcium imaging signals in neuronal cultures. *Front Neural Circuits* 2013;7:199.
- Toga AW, Thompson PM, Mori S, Amunts K, Zilles K. Towards multimodal atlases of the human brain. *Nat Rev Neurosci* 2006;7:952–66.
- Tomek J, Novak O, Syka J. Two-photon processor and SeNeCa – a freely available software package to process data from two-photon calcium imaging at speeds down to several ms per frame. *J Neurophysiol* 2013;110:243–56.
- Tsubo Y, Isomura Y, Fukai T. Neural dynamics and information representation in microcircuits of motor cortex. *Front Neural Circuits* 2013;7:85.
- Turrigiano G, Abbott LF, Marder E. Activity-dependent changes in the intrinsic properties of cultured neurons. *Science* 1994;264:974–7.
- Uhlhaas PJ, Haenschel C, Nikolic D, Singer W. The role of oscillations and synchrony in cortical networks and their putative relevance for the pathophysiology of schizophrenia. *Schizophr Bull* 2008;34:927–43.
- Uhlhaas PJ, Singer W. Neural synchrony in brain disorders: relevance for cognitive dysfunctions and pathophysiology. *Neuron* 2006;52:155–68.
- Caselles V, Kimmel R, Sapiro G. Geodesic active contours. *Int J Comput Vis* 1997;22:61–79.
- Voigt T, Opitz T, de Lima AD. Activation of early silent synapses by spontaneous synchronous network activity limits the range of neocortical connections. *J Neurosci* 2005;25:4605–15.
- Watts DJ, Strogatz SH. Collective dynamics of ‘small-world’ networks. *Nature* 1998;393:440–2.
- Womelsdorf T, Schoffelen JM, Oostenveld R, Singer W, Desimone R, Engel AK, et al. Modulation of neuronal interactions through neuronal synchronization. *Science* 2007;316:1609–12.
- Yaksi E, Friedrich RW. Reconstruction of firing rate changes across neuronal populations by temporally deconvolved Ca²⁺ imaging. *Nat Methods* 2006;3:377–83.
- Yamada J, Okabe A, Toyoda H, Kilb W, Luhmann HJ, Fukuda A. Cl⁻ uptake promoting depolarizing GABA actions in immature rat neocortical neurones is mediated by NKCC1. *J Physiol* 2004;557:829–41.
- Yoshiyama Y, Higuchi M, Zhang B, Huang SM, Iwata N, Saido TC, et al. Synapse loss and microglial activation precede tangles in a P301S tauopathy mouse model. *Neuron* 2007;53:337–51.
- Zariwala HA, Borghuis BG, Hoogland TM, Madisen L, Tian L, De Zeeuw CI, et al. A Cre-dependent GCaMP3 reporter mouse for neuronal imaging *in vivo*. *J Neurosci* 2012;32:3131–41.
- Ziv Y, Burns LD, Cocker ED, Hamel EO, Ghosh KK, Kitch LJ, et al. Long-term dynamics of CA1 hippocampal place codes. *Nat Neurosci* 2013;16:264–6.